INTERNATIONAL JOURNAL FOR NUMERICAL METHODS IN FLUIDS, VOL. 12, 143–160 (1991)

ADAPTIVE GRID COMPUTATION OF THREE-DIMENSIONAL NATURAL CONVECTION IN HORIZONTAL HIGH-PRESSURE MERCURY LAMPS

P. Y. CHANG

Advanced Technology Department, GE Lighting, Cleveland, OH 44112, U.S.A

AND

W. SHYY

Department of Aerospace Engineering, Mechanics and Engineering Science, University of Florida, Gainesville, FL 32611, U.S.A.

SUMMARY

A three-dimensional model has been developed to compute the thermofluid transport within a discharge arctube. The model has proved very useful for guiding the choice of design parameters to optimize the lamp performance. However, uncertainties exist with respect to quantitative aspects of the physical model, especially those related to radiation heat transfer. In the present work a grid refinement procedure and an adaptive grid method are used to improve the quantitative accuracy of the model and to help improve the physical modelling. The adaptive grid method, based on the multiple one-dimensional equidistribution concept, can responsively redistribute the grids to optimize the grid resolutions. Adaptive grid solutions modify the predicted maximum gas temperature, the buoyancy-induced convection strength, the location of the high-temperature core, and the wall temperature profiles. The adaptive grid solutions show more consistent trends when compared to the measurements. On the basis of the quantitatively more definite information, adjustments can be made with regard to the uncertainties of the physical model.

KEY WORDS Adaptive grid computation Natural convection Navier–Stokes flow Curvilinear coordinates

1. INTRODUCTION

The important effect of convection on the heat transfer rate and overall performance of a high-pressure discharge lamp has now been well recognized.[1–6] Until very recently, research on convection transport within the discharge lamp has been based largely on experimental or empirical approach.[1] Zollweg[2] and Lowke[3] were the first to conduct the analytical and computational study of this important process based on first principles. In References 2 and 3 the fluid flow and energy equations in an axisymmetric domain are solved. Recently, progress has been made along the line of computational modelling in a three-dimensional domain[4–6] with the capability of handling the irregular and complex geometry of the arctube, including the curved surface and electrode insertion. The model advanced in References 4–6 solves the combined momentum, mass continuity, energy and electric field, based on first principles, and simplified radiation transfer equations using a finite volume algorithm in general curvilinear co-ordinates.[7–9] Both straight and curved arctubes have been studied and their impact on overall performance predicted. Good agreements have been obtained in terms of mounting angle,[4,6] curvature effect[5] and wall temperature distribution.[6] These favourable agreements indicate that

0271–2091/91/020143–18$09.00
© 1991 by John Wiley & Sons, Ltd.
Received 16 August 1989
Revised 8 November 1989

the computational model based on first principles and simplified modelling can make a truly useful contribution by guiding the choice of design parameters to optimize lamp performance, at least in a qualitative way. In fact, useful information has already been supplied to the designers for understanding the flow and thermal phenomena occurring in the discharge arc and for improving the design.

We are, of course, also well aware of the fact that the combined mass, momentum, energy and electricity transport process in the arctube is an extremely complicated one. Many uncertainties are present in the modelling process, as briefly discussed in Reference 6. For instance, one of the major difficulties is the appropriate treatment of radiation heat transfer. Since the plasma arc temperature within the arctube can approach or exceed 7000 K, the radiation transfer mode is expected to play a very important role. Unfortunately, owing to the large degree of geometric complexity in the curved arctube, a preferred shape for the horizontal mounting position, it is not practical to do a detailed computation of the radiation transfer in three dimensions. In References 4–6 a much simplified treatment has been used. It requires the prescription of adjustable parameters such as the absorption coefficients of radiation in the colder mercury vapour and by the wall. There is not enough information for one to determine these coefficients *a priori*. For instance, in References 4–6 the coefficients are determined first by limited empirical information and then adjusted by inspecting the differences between the predicted and measured temperatures. Although it has been found that qualitatively the results predicted in References 4–6 are not sensitive to these adjustable parameters, exact quantitative solutions are obviously dependent upon the choice of them.

It is noted that in References 4–6 relatively coarse grid systems with $29 \times 13 \times 13$ and $29 \times 17 \times 13$ grid points were employed. Since the Grashof number is estimated to be of the order of 10^5, it is expected that a more refined treatment of the grid system is needed in order to obtain numerically definite solutions. It is on the basis of this background that we have embarked on the present study. The goal is to increase the number of grid points on one hand and to utilize the available amount of grid points as effectively and optimally as possible. Once a numerically more definite solution is achieved, one can better assess the appropriate choice of adjustable parameters introduced in the simplified models.

The approach undertaken in the present study is to employ an adaptive grid computational method developed and successfully applied earlier[10–12] to help optimize the grid distribution within the arctube. The curved arctube studied in Reference 6 is chosen as the model here since a substantial amount of information is available both theoretically and experimentally. Four different systems with different distributions as well as total numbers of grids (ranging from $29\times17\times13$ to $29\times29\times29$) have been used here.

2. ARCTUBE GEOMETRY AND PROBLEM FORMULATION

The geometrical definitions of the arctube along with electrodes are given in Figure 1(a). Schematic illustrations of two-dimensional representation grid projections of one middle side-view plane, one cross-section plane containing the electrode and the middle cross-section plane of symmetry are shown in Figures 1(b)–1(d) respectively. Three-dimensional illustrations of the curved arctube under study are shown in Figures 1(e) and 1(f). Table I shows the geometric input data for the arctube used here. The input power and mercury pressure are 400 W and 3 atm respectively.

To resolve the geometrical complexities of the arctube and electrodes, the transport equations are solved by an algorithm developed for solving Navier–Stokes flows using general non-orthogonal curvilinear co-ordinates.[7–9] The volumetric source-terms driving the flow are ohmic

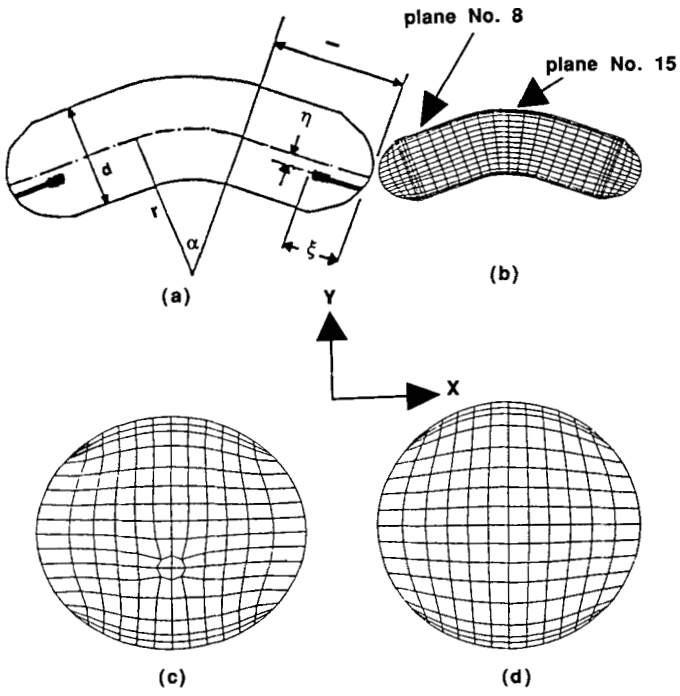

Figure 1. (a) Arctube design with symmetrical bowl ends. (b) Corresponding computer-generated geometry and mesh. (c) Mesh of a cross-section containing the electrode. (d) Mesh of the middle cross-section plane

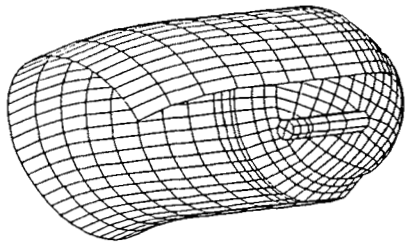

Figure 1(e). Half of the arctube with the front wall removed (in 3D perspective)

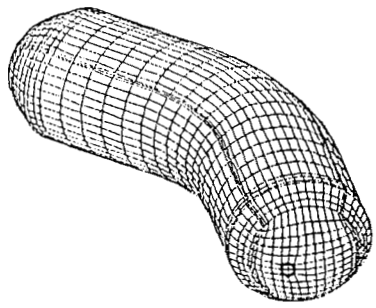

Figure 1(f). Computer-generated geometry and mesh (in 3D perspective)

Table I. Model input

Symbol	Geometric design parameters	400 W curved arctube model data
d	Arctube diameter (mm)	15·1
l	Arctube length (mm)	59·3
ξ	Electrode insertion length (mm)	9·3
η	Offset electrode distance (mm)	2·3
r	Radius of bend (mm)	25·4
α	Angle of bend (deg)	40
t	Wall thickness (mm)	1·2

heating and radiation cooling, which enter the energy equation, and gravitation, which enters the momentum equations.

The governing equations are first written in the strong conservation law form in Cartesian co-ordinates for the dependent variable ϕ:

$$\frac{\partial}{\partial x}(\rho u\phi)+\frac{\partial}{\partial y}(\rho v\phi)+\frac{\partial}{\partial z}(\rho w\phi)=\frac{\partial}{\partial x}\left(\Gamma\frac{\partial\phi}{\partial x}\right)+\frac{\partial}{\partial y}\left(\Gamma\frac{\partial\phi}{\partial y}\right)+\frac{\partial}{\partial z}\left(\Gamma\frac{\partial\phi}{\partial z}\right)+R(x, y, z). \quad (1)$$

Here Γ is the effective diffusion coefficient and R is the source term, including the gravitational force in the momentum equation, and ohmic heating and radiation transfer effects in the energy equation. Equation (1) can represent the continuity, momentum, energy and electric field equations (equation (2)). When new independent variables ξ, η and γ are introduced, equation (1) changes according to the general transformation $\xi=\xi(x, y, z), \eta=\eta(x, y, z), \gamma=\gamma(x, y, z)$. The result of this co-ordinate transformation is to transform the arbitrarily shaped physical domain into a rectangular parallelepiped.

The electric field equations can be expressed in terms of electrostatic potential in the form

$$\nabla\cdot\sigma\nabla\Phi=0. \quad (2)$$

Here σ is the electrical conductivity and Φ is the electrostatic potential. It should be noted that the strong temperature dependence of the electrical conductivity produces a strong coupling between the electric field equations and the thermofluid transport equations. This is especially true near the electrode tips, where this coupling is responsible for attaching the arc to the electrode tips. The full treatment of gas-to-gas radiation is very complex and is not practical for three-dimensional problems because the necessary computations would consume enormous computer time. The simplified treatment is given by

$$\text{radiant heat loss}=A_{\text{urad}}+1{\cdot}425\times10^{-14}\exp(C/T), \quad (3)$$

where $C=-8{\cdot}0661\times10^{4}$; T is temperature and A_{urad} is a constant which represents the energy (per unit volume) absorbed in the cold gas region.

Boundary conditions are imposed at the quartz wall of the arctube and the surfaces of the electrodes. For the fluid flow calculation, conventional no-slip boundary conditions are applied on the entire boundary for the velocity components. For electric field calculations the electrodes have surfaces of uniform electrostatic potential and the normal component of the current density is zero at the wall.

The temperature distribution of the quartz inner wall is determined by the energy balance, equation (4), at the gas–wall boundary, which consists of three terms: the energy conducted to the

wall by the gas, the radiant energy absorbed by the wall and the energy conducted through the arctube wall. The temperature distribution of the quartz outer wall is determined by the energy balance, equation (5), at the arctube outer boundary, which consists of two terms: the energy conducted to the outer boundary through the wall thickness and the energy radiated by the wall. The above terms are formulated as

energy (per unit area) conducted to wall by gas: $-k_{\text{gas}}\dfrac{T_{\text{w}}-T_{\text{P}}}{\delta}$,

radiant energy (per unit area) absorbed by wall: CR,

energy (per unit area) conducted through wall thickness: $-k_{\text{qtz}}\dfrac{T_{\text{qtz}}-T_{\text{w}}}{t}$,

energy (per unit area) radiated by wall: $\sigma\varepsilon(T_{\text{qtz}}^4-T_{\text{sink}}^4)$,

$$-k_{\text{gas}}\frac{T_{\text{w}}-T_{\text{P}}}{\delta}+CR=-k_{\text{qtz}}\frac{T_{\text{qtz}}-T_{\text{w}}}{t}, \tag{4}$$

$$-k_{\text{qtz}}\frac{T_{\text{qtz}}-T_{\text{w}}}{t}=\sigma\varepsilon(T_{\text{qtz}}^4-T_{\text{sink}}^4), \tag{5}$$

where k is the thermal conductivity, which is a function of temperature, T is the temperature in K, 'P' stands for the centre of a control volume, 'w' stands for the quartz inner wall, δ is the normal distance from the centre of the fluid control volume to the wall, C is the fraction of radiation impinging on the wall that is absorbed, R is the radiation impinging on the wall per unit area, 'qtz' stands for quartz, T_{sink} is the outer jacket wall temperature, t is the quartz wall thickness, σ is the Stefan–Boltzmann constant and ε is the quartz emissivity, which is a function of temperature.

Order-of-magnitude analysis indicates that as far as conduction in the wall is concerned, the radial direction is the only dominant one. Conduction along both the longitudinal and circumferential directions of the wall is negligible.

An accurate treatment of the radiant energy absorbed by the wall is a difficult task owing to the irregular 3D geometry and the moving hot arc position during iterative calculation. The fraction of radiation impinging on the wall that is absorbed is also difficult to determine. Theoretically it depends on wavelengths as well as on temperature. To obtain an approximate treatment of this term, view factors from the hot arc to the inner wall were calculated from the software RAVFAC, documented in a NASA contractor report.[13] The geometry of the curved arctube was treated as a cylinder with flat end-caps and the hot arc considered as a much smaller concentric cylinder between the electrode tips within the arctube.[6]

Both measurements and calculations of the outer quartz wall temperatures were conducted with a vacuum outer jacket so that the convection effect outside the arctube is not present.

The convective flow in the discharge is assumed to be purely laminar; this assumption is supported by both the experimental evidence and the calculated Grashof number. For all the derivatives in the transport equations, convection terms included, the second-order central differencing scheme is employed for discretization. A multigrid method is employed for solving the resulting difference equations. In the following, the basic idea of the adaptive grid computation and specific features adopted in the present work are given.

The most appealing aspect of the adaptive grid method is that the grid distribution can be adjusted in an intelligent way without resorting to *a priori* knowledge and/or the intuition of the user, and hence one can reduce the size of the grid system that is needed to yield an accurate

solution. This was exemplified in the study conducted by DeVahl Davis and Jones.[14] In comparing the various numerical methods submitted by many individuals for calculating the natural convection in a square cavity, they found that, to their surprise, the use of a non-uniform grid distribution generated by intuition did not, on the whole, yield better numerical accuracy than that of a uniform grid distribution. This finding demonstrates that while a denser distribution of mesh points in 'suitably chosen' locations should lead to improved accuracy, how to choose such suitable locations and the effects of the consequently coarsened grid distribution elsewhere on the numerical accuracy must be considered carefully.

For multidimensional Navier–Stokes flow, effective application of the adaptive grid method cannot be made unless issues such as the different characteristics of the dependent variables in a coupled system of equations, the non-linear behaviour of the flow and extra complexities introduced by the non-regular flow configurations are appropriately resolved. Several methods have been proposed in the literature to utilize the adaptive grid method for fluid flow computation. For example, Dwyer *et al.*,[15] Rai and Anderson,[16] Bell and Shubin,[17] Nakahashi and Deiwert[18] and Ghia *et al.*[19] have demonstrated the effectiveness of their method with different formulations. Anderson,[20] Thompson[21] and Eiseman[22] have given comprehensive surveys of this topic with many relevant references. Here we have adopted an adaptive method developed earlier[10–12] which is based on the concept of multiple one-dimensional equidistribution. The method has been found to yield characteristics of error reduction that are consistent with analytical work of Babuska and Rheinboldt.[23] Several successful applications have also been demonstrated with interesting features presented.

The basic idea developed there also accounts for the important fact that for the Navier–Stokes equations the various dependent variables can have different characteristics, depending on the flow configurations.

The adaptive grid method is based on the idea that grid points will be distributed along a given arc length in space, depending on the weighting function. The mathematical expression of this idea is as follows:

$$\xi = \xi_{\max} \frac{\int_0^s W \, ds}{\int_0^{s_{\max}} W \, ds}, \tag{6}$$

where ξ is the general co-ordinate, W is the weighting function used to adapt the grid distribution, s is the arc length and $s_{\max}$ is the maximum arc length. If ξ is incremented with a constant value, equation (6) implies that

$$W_i \Delta s_i = \text{constant} \quad \text{for all } i, \tag{7}$$

where i is the nodal number of the discrete grid points, Δs_i is the interval along the given arc and W_i is the corresponding weighting function in the interval. There are many ways to construct the weighting function, such as taking into account the relative importance of three factors: (a) total arc length (smoothing term), (b) dependent variable function variation (first derivative) and (c) dependent variable slope variation (second derivative). In general, W can be written as

$$W = a + f(\phi_s, \phi_{ss}, \ldots). \tag{8}$$

The numerical procedure used in References 10–12 was that the grid adaptation starts with the uniform grids and the numerical solutions obtained on them. The uniform grid solution is used to estimate W and the new grid positions are determined from the following equation, which is

equivalent to equation (6):

$$\int_0^{s_i} W \mathrm{d}s = \frac{\xi_i}{\xi_{\max}} \int_0^{s_{\max}} W \mathrm{d}s, \tag{9}$$

with ξ incremented uniformly from one grid to the next. By solving equation (9), the grid positions of the s_i can be determined one by one. The new grid positions are then in turn used to recalculate the numerical solution of the Navier–Stokes and associated transport equations.

It has been demonstrated that one advantage of this *a posteriori* multiple one-dimensional adaptive grid method is its flexibility and ease in adding grid points along the co-ordinate lines if desired.[10] It was also shown that in the multistage adaptive grid procedure the resulting grid system is already close to optimum after a few stages of adaption. Furthermore, as the adaptive readjustment of the grid distribution proceeds from the initial grid system, not only is the overall error reduced but the error distribution appears more uniform.[11,23] The present adaptive grid method has been applied to compute the two-dimensional natural convection problem.[12] Comparisons of the solutions on uniform and adaptive grids with the reported benchmark results have demonstrated the important contributions the adaptive grid method can make in resolving complicated flow characteristics.

One important issue of the adaptive grid computation is the possible appearance of highly skewed meshes in the flow domain. In this regard, several treatments can be employed. In Reference 12 a combined use of variational type of adaptive grid formulation as a postprocessing treatment in conjunction with the aforementioned multiple one-dimensional procedure has been found effective for the natural convection flow within an enclosure. In the present study it is found that a straightforward implementation of the aforementioned multiple one-dimensional adaptive grid method can be utilized without the adverse effect of grid skewness. The present work also represents the first three-dimensional application of the present adaptive grid method.

3. RESULTS AND DISCUSSION

Four grid systems with different distributions and numbers of nodal points are employed. The coarsest mesh system, with $29 \times 17 \times 13$ nodal points, as shown in Figure 2(a), is the same one as used in Reference 6, in which a largely uniform mesh distribution is given except near the top and bottom wall regions where the meshes are locally more refined than in the other regions. A grid system of $29 \times 19 \times 19$ nodal points and smooth mesh spacings without adaptive local grid clustering is shown in Figure 2(b). The finest mesh systems contain $29 \times 29 \times 29$ nodal points. Figure 2(c) shows the smooth grid system. Based on the solution obtained on Figure 2(c), an adaptive grid system is generated as shown in Figure 2(d). In the adaptive procedure the weighting function is of the form

$$W = a + \left|\frac{\partial T}{\partial s}\right| + \left|\frac{\partial (T^5)}{\partial s}\right|. \tag{10}$$

Here the weighting function is comprised of the linear and non-linear contributions from the temperature field in order to cluster the nodal points more responsively.

The formula of equation (10) was chosen to balance the competing features of the high-temperature gas in the core region, which is around 7000 K, and the much colder wall region, which is less than 1000 K. The hot gas core needs good mesh resolution because the strength of convection field is determined largely by the temperature and density gradients there. The wall region also needs good mesh resolution because the overall heat transfer rate, which is determined

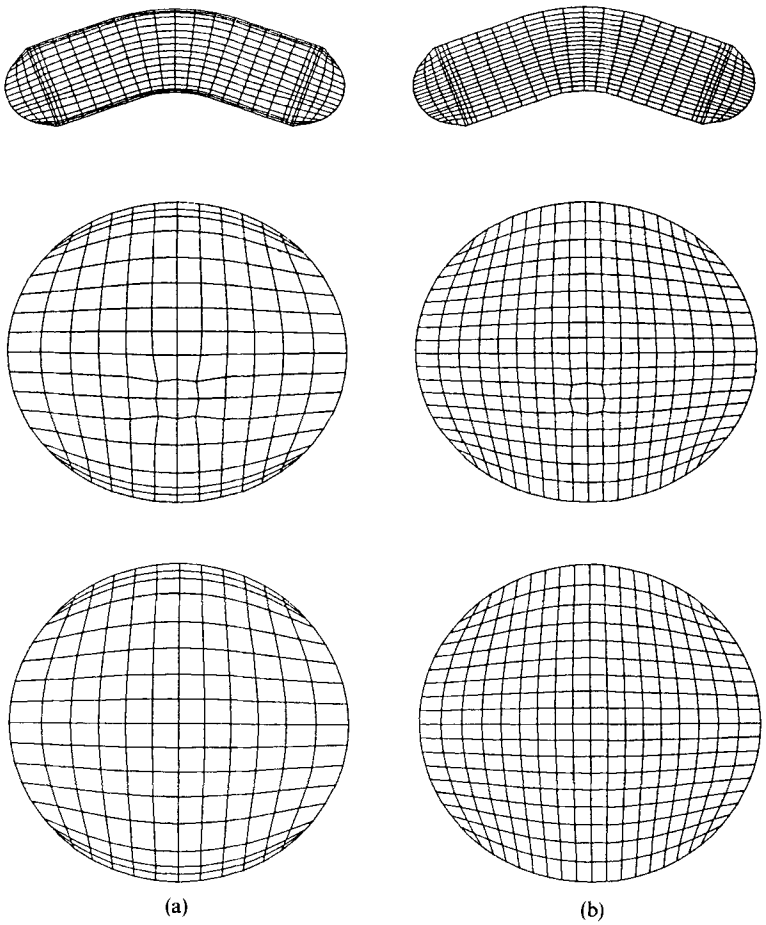

Figure 2. Top: middle side-view plane (plane of symmetry). Middle: cross-section plane no. 8. Bottom: middle cross-section plane (plane no. 15). (a) 29 × 17 × 13 non-adaptive grids. (b) 29 × 19 × 19 non-adaptive grids.

by estimating the temperature gradient, is determined as part of the boundary conditions. Furthermore, since in the present applications the wall temperature distribution is of critical importance to the design optimization, accurate numerical values of wall temperature profile are part of the key output of the prediction. The combination of the linear ($\partial T/\partial s$) and non-linear ($\partial T^5/\partial s$) terms was designed to compromise this need. The non-linear term of the weighting function formulation can also partially accommodate the extremely non-linear variation of the source term in the energy equation arising from the radiation heat transfer model. As to the smoothness factor in equation (10), there is no known value that is uniquely suited. Our experience has suggested that any number of order unity is acceptable. The adaptive remeshing is conducted with the aforementioned multiple one-dimensional procedure on each cross-section plane sequentially. More specifically, the basic process as it takes place in each cross-section plane is a four-step one: the solution of temperature obtained on the original grid system as shown in Figure 2(c) is extracted; the temperature field is normalized by the maximum magnitude presented in the individual cross-section plane; the adaptive remeshing process is conducted along the two family co-ordinate lines sequentially according to the weighting function (equation (10)) with $a = 3$; solutions of all other flow variables are extracted and interpolated (including

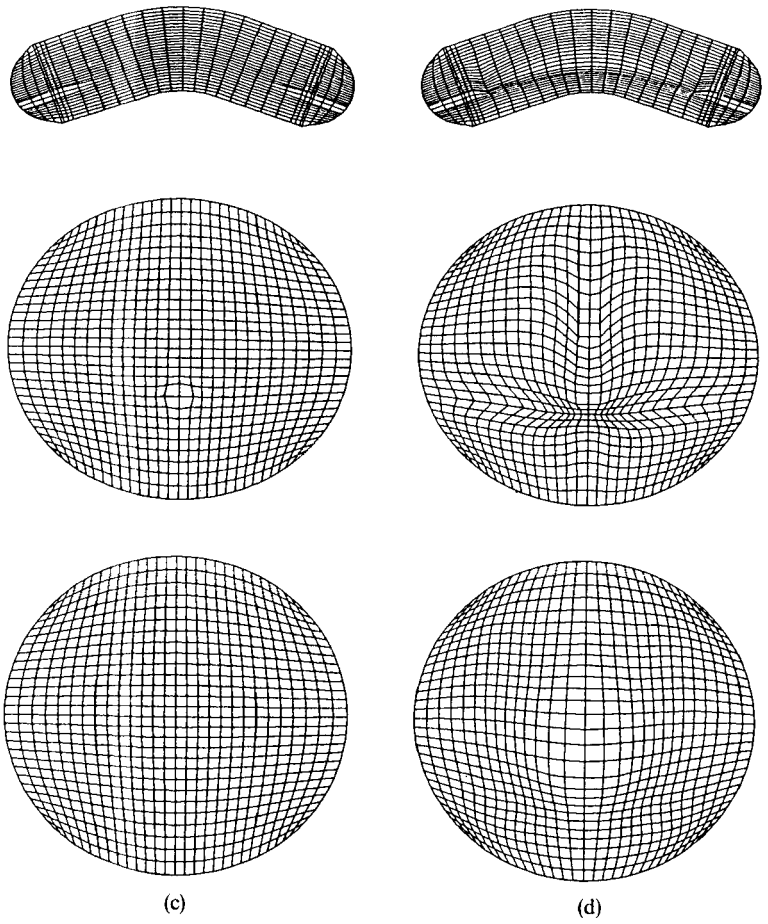

Figure 2 (continued). (c) 29 × 29 × 29 non-adaptive grids. (d) 29 × 29 × 29 adaptive grids.

temperature) on the newly redistributed grid as shown in Figure 2(d). After all cross-section planes have been processed one by one in this orderly manner, the new grid and flow variables are then used by the flow solver to continue the computation.

All the computations reported in the present work were conducted on a VAX/8600 computer. A solution is considered to be converged if the overall residual from the continuity, momentum and energy equations, defined as the absolute sum of the residuals of all the finite volumes, is smaller than 10^{-7}. A typical calculation requires about 800 iterations of a 29 × 17 × 13 grid system. A two-level multigrid method has been used to solve the pressure correction equation, while a point SSOR method has been used to solve the other transport equations to optimize the computational effort. In terms of CPU time, with a 29 × 17 × 13 grid system it takes 1·4 h for every 100 global iterations. The present adaptive grid method utilizes a sequential approach; however, the solution based on the original initial grid system need not be solved to very high accuracy. As stated earlier, the adaptive grid distribution, with the aid of the smoothness term, is reasonably insensitive to low-level noises of the solution. In the present case, since the flow field is induced by the temperature non-uniformity, the grids obviously should reflect the temperature field faithfully. As will become clear later on, the grids shown in Figure 2(d) do reflect the characteristics of the temperature field. For example, in the cross-section plane no. 8, which is

close to the tip of the electrode, substantially refined grid resolutions have been produced in the lower central domain where the high electric field adjacent to the electrodes heats up the gas substantially. In the cross-section plane no. 15, which is the plane of symmetry, the grids tend to show opposite features, namely the central domain is of coarser meshes while the outside region is of finer meshes. This feature is caused by the situation that although the temperature in the core is very high, it is relatively smooth in distribution. In the wall region, on the other hand, there is a substantial temperature gradient owing to the large heat transfer rate across the arctube wall. The middle side-view plane reveals the same characteristics from a different viewpoint, which shows more concentrated grid distributions in the region of high temperature gradients. The various features of the computed velocity and temperature fields on the four different grid systems will be assessed and compared next.

Figure 3 compares the temperature contours of the middle side-view plane obtained on the four grid systems. All four solutions are qualitatively very similar, thus rendering the credibility of the results presented in References 4–6. Nevertheless, there are discernible differences in terms of the quantitative distributions shown in Figure 3. On the smooth grid systems the maximum gas temperature increases monotonically as the number of grids increases, i.e. from 6931 K ($29 \times 17 \times 13$ grids) to 7096 K ($29 \times 19 \times 19$ grids) to 7165 K ($29 \times 29 \times 29$ smooth grids). With the use of the adaptive grid procedure the grid distribution is responsive to the temperature characteristics. However, the adaptive grid solution shows that the maximum gas temperature is 6938 K, which is very close to that of $29 \times 17 \times 13$ non-adaptive grids. Inspections show that the contributing factors to the same level of maxinum gas temperature obtained on the coarse non-adaptive grids and the fine adaptive grids are different. As will be demonstrated in the following, the intrinsic three-dimensionality of the transport characteristics is mostly responsible for the phenomenon. It also illustrates the difficulty that one may encounter in accurately modelling and computing the present three-dimensional thermofluid transport process.

Table II and Figures 4 and 5 summarize the major information on the velocity components along the horizontal (axial) and vertical co-ordinates and the range of temperature distribution in the cross-section plane no. 8, which is next to the electrodes. Because the flow field is highly three-

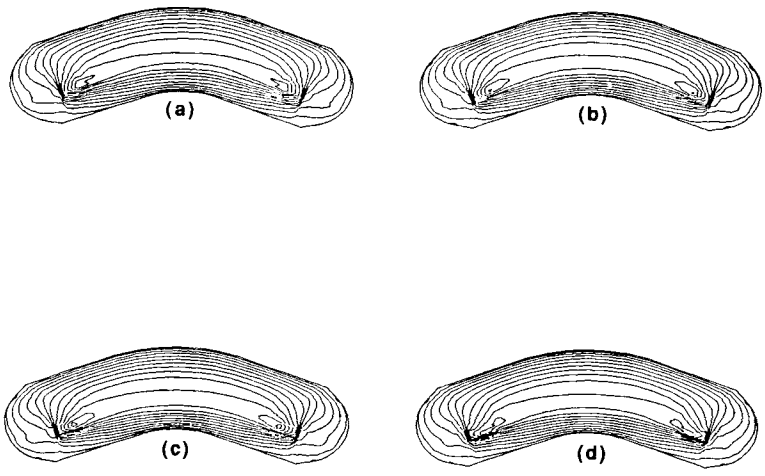

Figure 3. Temperature contours in the middle side-view planes (planes of symmetry): (a) $29 \times 17 \times 13$ non-adaptive grids, max. temperature 6931 K; (b) $29 \times 19 \times 19$ non-adaptive grids, max. temperature 7096 K; (c) $29 \times 29 \times 29$ non-adaptive grids, max. temperature 7165 K; (d) $29 \times 29 \times 29$ adaptive grids, max. temperature 6938 K

Table II. Velocity and temperature fields in cross-section plane no. 8 (adjacent to the electrodes)

Grid	V_x (cm s^{-1})			V_y (cm s^{-1})			T (K)		
	Min.	Max.	Overall strength (max. − min.)	Min.	Max.	Overall strength (max. − min.)	Min.	Max.	Max. − Min.
29 × 17 × 13, non-adaptive	−9·89	9·52	19·41	−3·63	21·30	24·93	751	6931	6180
29 × 19 × 19 non-adaptive	−10·12	10·17	20·29	−4·12	20·46	24·58	779	7096	6317
29 × 29 × 29, non-adaptive	−10·58	10·22	20·80	−4·20	20·42	24·62	774	7165	6391
29 × 29 × 29, adaptive	−10·40	10·35	20·75	−4·29	17·90	22·19	778	6938	6160

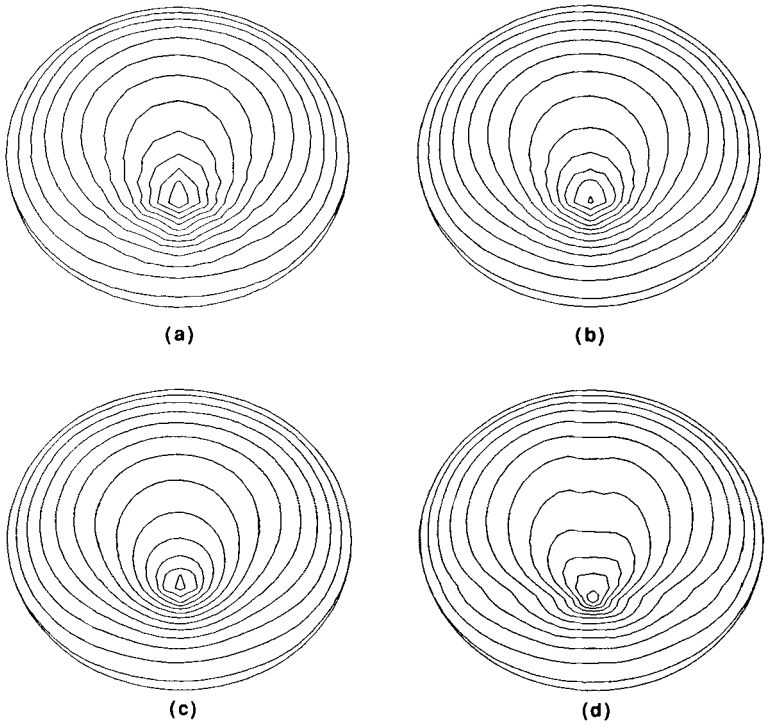

Figure 4. Temperature contours in cross-section plane no. 8 (adjacent to the electrodes): (a) 29 × 17 × 13 non-adapative grids, max. temperature 6931 K; (b) 29 × 19 × 19 non-adaptive grids, max. temperature 7096 K; (c) 29 × 29 × 29 non-adaptive grids, max. temperature 7165 K; (d) 29 × 29 × 29 adaptive grids, max. temperature 6938 K

dimensional, various factors such as arctube curvature, buoyancy and electric discharge interact with one another in complicated manners. As evidenced in Table II, one of the salient features depicted by the grid system is that as the grid resolutions are progressively improved by adding nodes and by adaptively redistributing nodes, the three-dimensionality of the flow field becomes more pronounced. The observation is supported by the fact that the overall strength of the

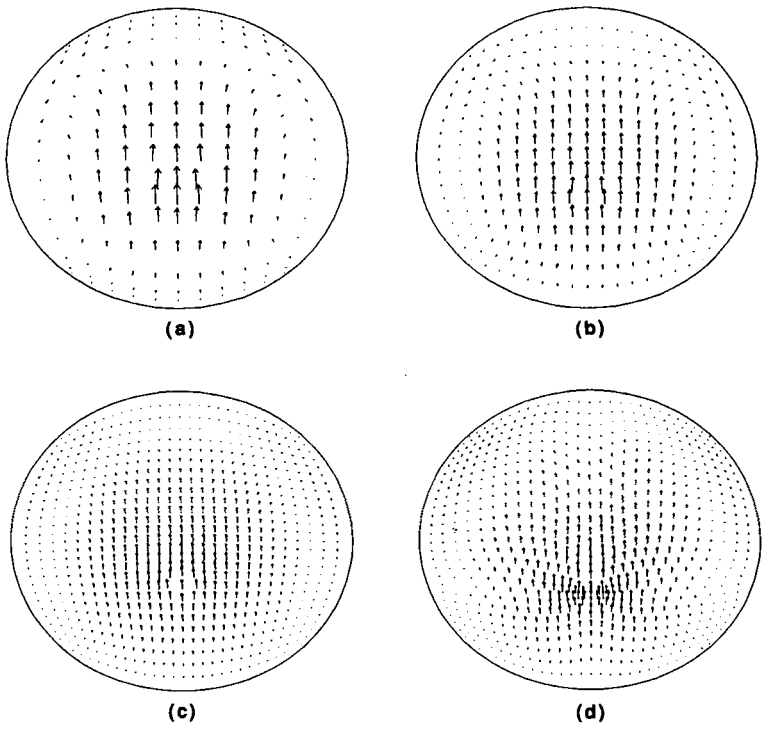

Figure 5. Velocity vectors in cross-section plane no. 8 (adjacent to the electrodes): (a) $29 \times 17 \times 13$ non-adaptive grids, max. $V_x = 9{\cdot}52\ \mathrm{cm\,s^{-1}}$, max. $V_y = 21{\cdot}3\ \mathrm{cm\,s^{-1}}$; (b) $29 \times 19 \times 19$ non-adaptive grids, max. $V_x = 10{\cdot}17\ \mathrm{cm\,s^{-1}}$, max. $V_y = 20{\cdot}46\ \mathrm{cm\,s^{-1}}$; (c) $29 \times 29 \times 29$ non-adaptive grids. max. $V_x = 10{\cdot}22\ \mathrm{cm\,s^{-1}}$, max. $V_y = 20{\cdot}42\ \mathrm{cm\,s^{-1}}$; (d) $29 + 29 + 29$ adaptive grids, max. $V_x = 10{\cdot}35\ \mathrm{cm\,s^{-1}}$, max. $V_y = 17{\cdot}90\ \mathrm{cm\,s^{-1}}$

horizontal velocity component (V_x) and the overall strength of the vertical velocity component (V_y), measured by the differences between the maximum and minimum values in plane no. 8, become progressively more comparable as the grid resolution improves.

With respect to the temperature field, no monotonic trend can be established in terms of the maximum temperature. Both the coarsest non-adaptive grid system with $29 \times 17 \times 13$ nodes and the adaptive grid system with $29 \times 29 \times 29$ nodes show more uniform temperature distribution. However, the reason for the uniformity of temperature distribution of the $29 \times 17 \times 13$ non-adaptive grids is inadequate grid resolution. The apparent closeness of temperature levels between the coarse non-adaptive and fine adaptive grid systems is coincidental. Figure 4 shows that the actual *distributions* of temperature contours between the two solutions are not the same. The location of the hot temperature core gradually but monotonically moves downwards as the grid resolution improves. The lower level of maximum temperature predicted by the coarse grid system is caused by inadequate grid resolution. The adaptive grid solution, on the other hand, predicts a stronger three-dimensional velocity field which results in a more effective transport process to reduce the maximum temperature. Furthermore, as will be shown in the following, these different mechanisms also cause the overall wall temperature distributions to be different on different grid systems.

It is also interesting to note that the convection strength of the gas flow does not necessarily correlate with the maximum gas temperature in a monotonic manner. One may expect that with the higher degree of heating associated with the better-resolved temperature field close to the tips

of the electrodes, the density non-uniformity increases, which should result in a stronger buoyancy effect on convection. However, there is a counteracting influence exerted by the temperature dependency of the viscosity. The formula adopted for computing the dynamic viscosity of mercury gas is as follows:

$$\mu = 2{\cdot}4789 \times 10^{-5} + 7{\cdot}64 \times 10^{-8} T + 1{\cdot}039 \times 10^{-3} \exp\left(-\frac{1{\cdot}4867 \times 10^{4}}{T}\right), \tag{11}$$

with the unit of $\mathrm{kg\,m^{-1}\,s^{-1}}$, where T is the gas temperature in K. It is also noted that the Prandtl number is taken to be a constant value of 0·61. The equation of state under constant pressure is

$$\rho = A/T + B, \tag{12}$$

where $A = 7{\cdot}122 \times 10^{3}\ \mathrm{kg\,m^{-3}\ K}$ and $B = -0{\cdot}0465\ \mathrm{kg\,m^{-3}}$. Hence, as the maximum temperature increases, both the dynamic viscosity and thermal diffusivity increase, resulting in a larger viscous and conductive effect on the transport process. In terms of the Grashof number

$$Gr = gd^{3}\Delta\rho/v^{2}\rho, \tag{13}$$

where g is the gravitational acceleration, d is the arctube diameter, ρ is the density of mercury gas and v is the kinematic viscosity of mercury gas, it is clear that as the temperature increases, the proportional increase in the dynamic viscosity reduces Gr in a non-linear manner. By taking full account of the gas property variations with respect to the temperature effect, the convection effect does not always necessarily increase with increasing temperature and density non-uniformities. One can actually observe an inverse relationship between the temperature variation and convection strength. This trend cannot be accounted for by the simplified Boussinesq approximation, which assumes that both the density and viscosity have constant values. Hence the effect of gas property variations on the convection strength cannot be properly incorporated by the Boussinesq approximation.

A representative illustration of the velocity vectors in the middle side-view plane is given in Figure 6. In the regions close to the electrodes the convection strengths along the axial direction, i.e. u-velocity, are comparable to those induced directly by gravity, i.e. v-velocity. In summary, there are several competing transport characteristics present in the whole domain, namely the electric current and resultant ohmic heating, the buoyancy effect in cross-section planes and the curvature of the arctube.

In the regions close to the electrodes the higher levels of temperature core there cause the transport process to be dominated by the combined effect of buoyancy and electric heating. Away

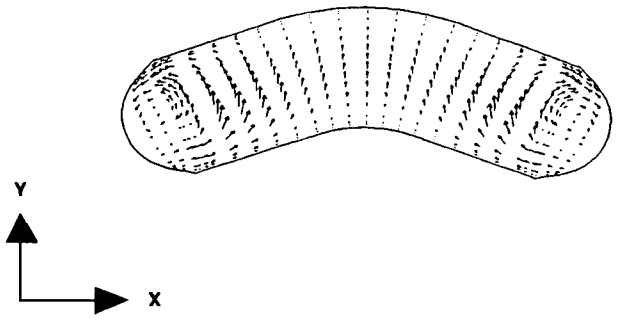

Figure 6. Velocity vectors in the middle side-view plane (plane of symmetry)

Table III. Velocity and temperature fields in cross-section plane no. 15 (plane of symmetry)

Grid	V_y (cm s^{-1})			T(K)			Hot core displacement (mm)
	Min.	Max.	Overall strength (max. − min.)	Min.	Max.	Max. − min.	
29 × 17 × 13 non-adaptive	−3·85	8·00	11·85	1049	6054	5005	−1·2
29 × 19 × 19, non-adaptive	−4·24	7·47	11·71	1112	6108	4996	−1·6
29 × 29 × 29, non-adaptive	−4·04	7·13	11·17	1112	6132	5020	−1·9
29 × 29 × 29, adaptive	−4.34	7.10	11.44	1103	6103	5000	−1·9

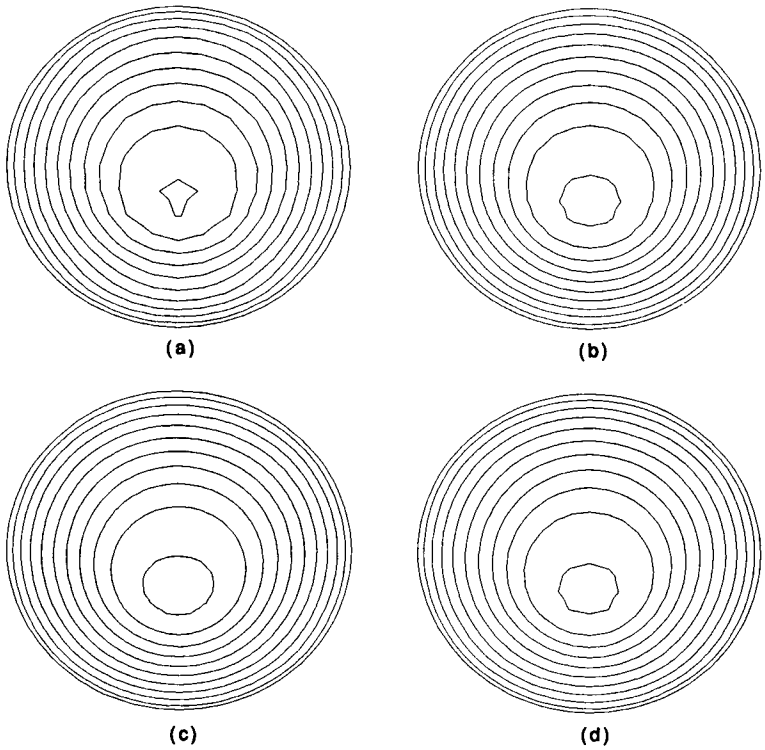

Figure 7. Temperature contours in the middle cross-section planes (planes of symmetry): (a) 29 × 17 × 13 non-adaptive grids, max. temperature 6054 K; (b) 29 × 19 × 19 non-adaptive grids, max. temperature 6018 K; (c) 29 × 29 × 29 non-adaptive grids, max. temperature 6132 K; (d) 29 × 29 × 29 adaptive grids. max. temperature 6103 K

from the electrodes the transport process is determined by the interactions of the physical and geometrical constraints. Consequently, the resulting pattern is complicated. Table III and Figures 7 and 8 compare the temperature and velocity distributions in the middle cross-section planes computed on the four grid systems. The hot core displacement is defined as the distance between the location of maximum gas temperature and the geometric centre of the cross-section.

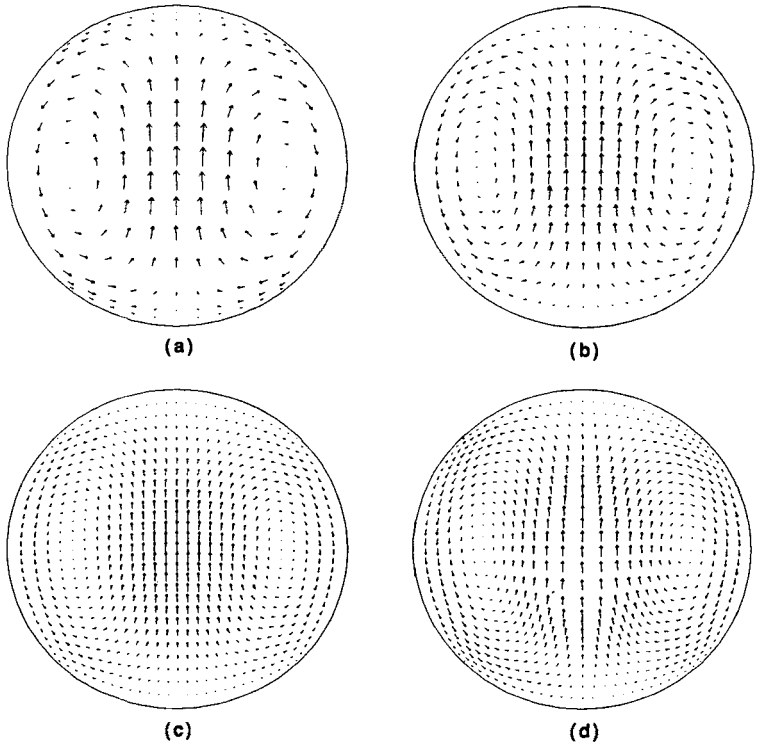

Figure 8. Velocity vectors in the middle cross-section planes (planes of symmetry): (a) 29 × 17 × 13 non-adaptive grids, max. $V_y = 8{\cdot}00\ \mathrm{cm\,s^{-1}}$; (b) 29 × 19 × 19 non-adaptive grids, max. $V_y = 7{\cdot}47\ \mathrm{cm\,s^{-1}}$; (c) 29 × 29 × 29 non-adaptive grids, max. $V_y = 7{\cdot}13\ \mathrm{cm\,s^{-1}}$; (d) 29 × 29 × 29 adaptive grids, max. $V_y = 7{\cdot}10\ \mathrm{cm\,s^{-1}}$

All four systems show very comparable features, both qualitatively and quantitatively. The maximum values of the predicted gas temperature vary by no more than 1·3%. One can also observe that among the three non-adaptive grid systems the coarse mesh system produces lower values of the maximum temperature in both the end regions and the middle regions owing to the less than adequate spatial resolution. As for the adaptive grid solution, it shows similar features to the non-adaptive grid solutions in terms of distribution. This is because in the middle plane the concentrated effects of the electrodes are diminished and consequently there is no sharp gradient present in the plane. Nevertheless, a trend can still be observed for the displacement distance of the high-temperature core with respect to the grid resolution, which appears to be influenced by the temperature characteristics in the electrode regions. As already noted, the fine and adaptive grid solutions predicted larger hot core displacement in the electrode regions.

Figure 8 shows the velocity vectors projected on the middle symmetry plane from the cross-sectional view. Again, qualitatively similar results are obtained on all four grid systems. Also, there is a discernible trend which shows that larger temperature variations do not always produce a stronger convection effect as a result of the strong temperature dependence of the mercury gas properties.

Finally, Figures 9(b) and 9(c) show the comparisons of the wall temperatures between the experimental measurement and numerical predictions. The profiles are for the wall temperature along the top and bottom symmetry lines, from left to right. Figure 9(a) indicates the locations where the measured and predicted data are compared. For the top wall temperature, fairly close

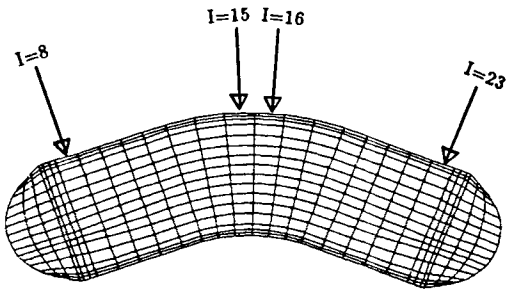

Figure 9(a). The I-locations in the middle side-view plane where the measured and calculated data are compared

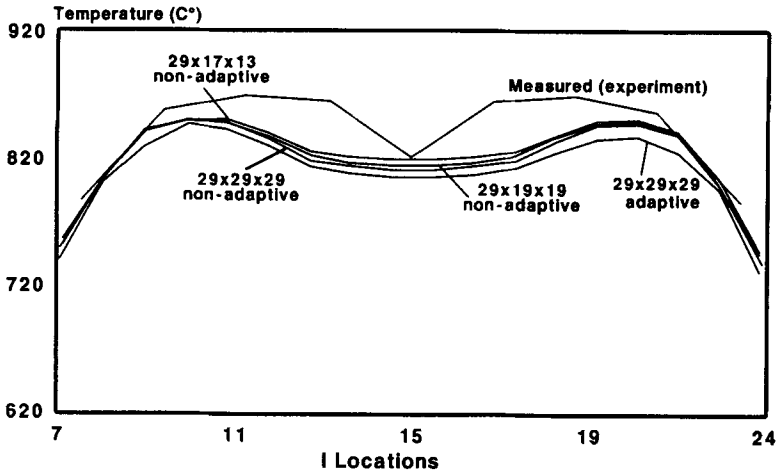

Figure 9(b). Temperature profiles of the top wall in the middle side-view plane

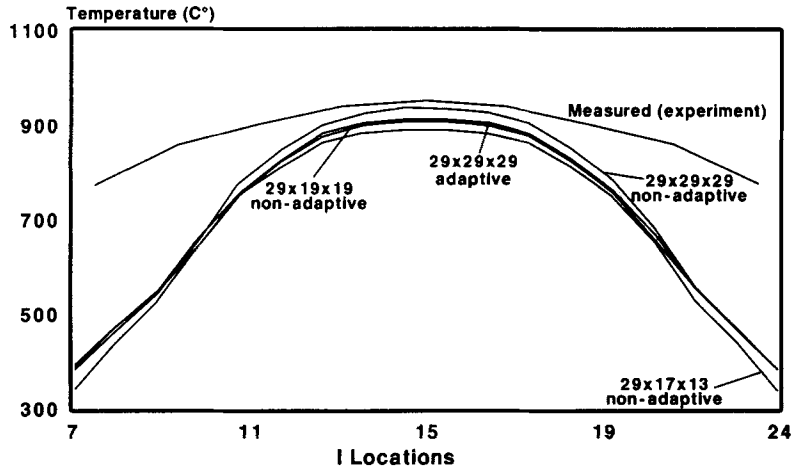

Figure 9(c). Temperature profiles of the bottom wall in the middle side-view plane

agreements have been obtained between the measurement and all of the predictions, except that the predicted centre top wall temperature depicts a trend of lower values with improved spatial resolution. More importantly, the overall variation of the top wall temperature becomes steeper as the grids are refined. For the bottom wall temperature the trend is no longer monotonic with respect to the grid spatial resolution. For the non-adaptive grid solutions there is a consistent trend which shows that the peak temperature on the bottom wall increases as the number of nodal points increases. The adaptive grid result shows a substantially different distribution. Its peak value is lower and its overall distribution is more moderate than the $29 \times 29 \times 29$ non-adaptive grid solution, hence depicting better agreement with the measurement. Compared to the non-adaptive grid system with the same number of nodes, the adaptive solution shows more consistent profiles qualitatively.

As already stated, large uncertainties may be contained in the physical submodules employed, especially the part of the radiation heat transfer. Hence what we have been striving to achieve in the present work is *not* to match the numerical values of the wall temperature profiles but to study the trend yielded by mesh improvement. For example, Figure 9(b) shows that the coarsest mesh system yields the best agreement with the measured top wall temperature profile; as the mesh distribution is improved, the agreement actually becomes worse. However, this feature should be combined with that of Figure 9(c), which shows that the coarsest mesh system yields the worst agreement with the measurement. The situation is opposite for the $29 \times 29 \times 29$ non-adaptive grid system, which shows the best match with the bottom wall temperature profile but the worst match with the top wall temperature profile. Thus, regardless of whether the radiation heat transfer increases or decreases its role, either one or other of the two wall temperatures comparisons will become worse. The adaptive grid solution, on the other hand, shows a more consistent trend. Comapred with the non-adaptive grid solution for the same number of nodes, the adaptive grid solution underpredicts the wall temperature profiles for *both* top and bottom walls. Hence it will allow room for adjusting and refining the physical models to improve the *overall* prediction capabilities.

4. CONCLUSIONS

On the basis of the present study, the following conclusions can be made.

1. The adaptive grid method can responsively reflect the solution profiles to optimize the grid resolutions. Large differences in grid distribution are observed in the region close to the electrodes where the finer meshes are clustered in the central portion, and in the region away from the electrodes where the finer meshes are distributed in the domain close to the wall.
2. In the end zone the dominant driving mechanism of the transport process is the buoyancy effect resulting from the electric heating. By exercising the grid dependence tests with four different grid systems of different distributions as well as numbers of nodal points, a clear trend is established for the convection pattern in the end zone. As the spatial resolution improves, the convection strength along the horizontal direction beocmes more comparable to that of the contra-rotating cells in the cross-sections. Consequently, the velocity field is more strongly three-dimensional in nature.
3. Since the present model fully accounts for the interdependence of the mercury gas properties with respect to the temperature effect, it is found that a higher temperature variation in a cross-section plane does not necessarily promote the convection strength. This result is caused by the strong effect of the temperature field on the viscocity and hence on the thermal conductivity.

4. The adaptive grid solution shows a reduced maximum gas temperature compared to the non-adaptive grid solutions with the same number of grid points. It predicts a more pronounced three-dimensional transport process which produces a more uniform gas temperature distribution. The qualitative agreements between adaptive grid solution and measurement for the wall temperature are more consistent in terms of overall trend.
5. With regard to the non-adaptive grid solutions, the coarser grid system predicts a lower maximum gas temperature in both the end region and the middle region owing to inadequate spatial resolution. Based on results presented here, adjustments can be made in the physical modelling aspects such as radiation heat transfer employed in the computation.

REFERENCES

1. W. Elenbaas, *Light Source*, Crane, Russak & Company, New York, 1972.
2. R. J. Zollweg, 'Convection in vertical high-pressure mercury arcs', *J. Appl. Phys.*, **49**, 1077–1091 (1978).
3. J. J. Lowke, 'Calculated properties of vertical arcs stabilized by natural convection', *J. Appl. Phys.*, **50**, 147–157 (1979).
4. W. Shyy and J. T. Dakin, 'Three-dimensional natural convection in a high-pressure mercury discharge lamp', *Int. Commun. Heat Mass Transfer*, **15**, 51–58 (1988).
5. P. Y. Chang, W. Shyy and J. T. Dakin, 'A study of three-dimensional natural convection in high pressure mercury lamps (part I: parameteric variations with horizontal mounting)', *Int. J. Heat Mass Transfer*, **33**, 483–493 (1990).
6. W. Shyy and P. Y. Chang, 'A study of the three-dimensional natural convection in high pressure mercury lamps (part II: wall temperature profiles and inclination angles)', *Int. J. Heat Mass Transfer*, **33**, 495–506 (1990).
7. W. Shyy, S. S. Tong and S. M. Correa, 'Numerical recirculating flow calculation using a body-fitted coordinate system', *Numer. Heat Transfer*, **8**, 99–113 (1985).
8. M. E. Braaten and W. Shyy, 'A study of pressure correction methods with multigrid for viscous flow calculations in non-orthogonal curvillinear coordinates', *Numer. Heat Transfer*, **11**, 417–442 (1987).
9. W. Shyy, S. M. Correa and M. E. Braaten, 'Computation of flow in a gas turbine combustor', *Combus. Sci. Technol.*, **58**, 97–117 (1988).
10. W. Shyy, 'An adaptive grid method for Navier–Stokes flow computation II: grid addition', *Appl. Numer. Math.*, **2**, 9–19 (1986).
11. W. Shyy, 'An adaptive grid method for Navier–Stokes flow computation', *Appl. Math. Comput.*, **21**, 201–219 (1987).
12. W. Shyy, 'Computation of complex fluid flows using adaptive grid method', *Int. j. numer. methods fluids*, **8**, 475–489 (1988).
13. J. K. Lovin and A. W. Lubkowitz, 'User's manual for RAVFAC (a radiation view factor computer program)', *NASA CR-61321*, 1969.
14. G. DeVahl Davis and I. P. Jones, 'Natural convection in a square: a comparison exercise', *Int. j. numer. methods fluids*, **3**, 227–248 (1983).
15. H. A. Dwyer, R. J. Kee and B. R. Sandere, 'An adaptive grid method for problems in fluid mechanics and heat transfer', *AIAA J.*, **18**, 205–212 (1980).
16. M. M. Rai and D. A. Anderson, 'Application of adaptive grids to fluid flow problems with asymptotic solutions', *AIAA J.*, **20**, 496–502 (1982).
17. J. B. Bell and G. R. Shubin, 'An adaptive grid finite difference method for conservation laws', *J. Comput. Phys.*, **52**, 569–591 (1983).
18. K. Nakahashi and G. S. Deiwert, 'A self-adaptive grid method with application to airfoil flow', *Proc. AIAA 7th Computational Fluid Dynamics Conf.* 1985, pp. 340–350.
19. K. Ghia, U. Ghia and C. T. Shin, 'Adaptive grid generation for flows with local high gradient regions', in K. Ghia and U. Ghia (eds), *Advances in Grid Generation, ASME-FED5*, ASME, New York, 1983, pp. 35–48.
20. D. A. Anderson, 'Adaptive grid methods for partial differential equations', in K. Ghia and U. Ghia (eds), *Advances in Grid Generation, ASME-FED5*, ASME, New York, 1983, pp. 1–15.
21. J. F. Thompson, 'A survey of dynamically adaptive grids in the numerical solution of partial differential equations', *Appl. Numer. Math.*, **1**, 3–27 (1985).
22. P. R. Eiseman, 'Adaptive grid generation', *Comput. Methods Appl. Mech. Eng.*, **64**, 321–376 (1987).
23. I. Babuska and W. C. Rheinboldt, 'Analysis of optimal finite-element meshes in R^1', *Math. Comput.*, **33**, 435–463 (1979).